



High-power Mg batteries enabled by heterogeneous enolization redox chemistry and weakly coordinating electrolytes

Hui Dong^{1,2,6}, Oscar Tutusaus^{3,6}, Yanliang Liang^{1,2}, Ye Zhang^{1,2}, Zachary Lebens-Higgins^{4,5}, Wanli Yang⁴, Rana Mohtadi³✉ and Yan Yao^{1,2}✉

Magnesium batteries have long been pursued as potentially low-cost, high-energy and safe alternatives to Li-ion batteries. However, Mg²⁺ interacts strongly with electrolyte solutions and cathode materials, leading to sluggish ion dissociation and diffusion, and consequently low power output. Here we report a heterogeneous enolization chemistry involving carbonyl reduction (C=O↔C-O⁻), which bypasses the dissociation and diffusion difficulties, enabling fast and reversible redox processes. This kinetically favoured cathode is coupled with a tailored, weakly coordinating boron cluster-based electrolyte that allows for dendrite-free Mg plating/stripping at a current density of 20 mA cm⁻². The combination affords a Mg battery that delivers a specific power of up to 30.4 kW kg⁻¹, nearly two orders of magnitude higher than that of state-of-the-art Mg batteries. The cathode and electrolyte chemistries elucidated here propel the development of magnesium batteries and would accelerate the adoption of this low-cost and safe battery technology.

The rapid growth and adoption of electrochemical energy storage in our society calls for developing next-generation batteries that combine high energy, high power and low cost. Among many post-lithium-ion batteries^{1–4}, rechargeable magnesium batteries utilizing divalent Mg²⁺ as charge carriers are expected to offer substantial improvements in volumetric energy density and affordability of batteries, due to the use of earth-abundant, high-capacity and safer dendrite-free Mg metal anode^{1,2,5,6}. However, power density has been the Achilles' heel of this technology.

The root cause of this challenge is intrinsic to divalent Mg²⁺ ion: it holds twice the amount of charge compared to Li⁺ while having a similar ionic radius. As a result, ion dissociation from electrolyte complexes and solid-state ion diffusion, two essential processes in classical intercalation chemistry, are sluggish at room temperature^{7–9}. Even state-of-the-art intercalation cathode materials, such as Mo₆S₈, require elevated temperatures to approach their theoretical capacity². Other cathode materials show fast kinetics at room temperature, notably organic polymers and layered compounds, but have been found to actually store partially complex ions, such as MgCl⁺ and solvated ions^{10–13}. While the storage of complex ions circumvents the dissociation and diffusion difficulties associated with Mg²⁺, it also brings new challenges: reduced practical cell-level energy density caused by its function as a hybrid battery or limited cycle life caused by volume changes in the electrode due to co-insertion of bulky solvent molecules^{10,14}. Cathode materials that can support fast Mg²⁺ storage would therefore require a new electrode reaction mechanism.

Electrolyte design plays an equally crucial role in improving battery kinetics. Historically, Mg electrolyte solutions hinged on the presence of chloride to increase salt solubility and improve the reversibility of Mg deposition/stripping¹⁵. While those remain in

the mainstream, efficient chloride-free electrolytes have recently been discovered, prompted by an urgency to overcome the serious challenges associated with chlorides, such as corrosion of current collectors and high dissociation energy of the Mg–Cl bond^{15–17}. Among these, the boron cluster-based electrolyte Mg(CB₁₁H₁₂)₂ (MMC) stands out as a widely recognized breakthrough in Mg electrolytes^{3,16}. MMC dissolves in oligomeric solvents, such as triglyme (G3) and tetraglyme (G4), to form some of the best-performing Mg electrolyte solutions in terms of reversibility of Mg deposition/stripping, electrochemical window, water stability and non-corrosivity¹⁶. Nevertheless, the high viscosity and strong coordination of higher glyme solvents are unfavourable for high power-density applications, because they lead to hindered ionic motion and slow kinetics at the electrolyte–electrode interface^{18,19}. Lower weight ether solvents, on the other hand, struggle to dissolve MMC¹⁶. A suitable solvent capable of fast ion conduction without compromising salt solubility remains a critical missing piece towards achieving a fast-kinetic Mg battery.

Here we report a strategy to overcome the challenges of ion dissociation and solid-state diffusion, whilst solely storing Mg²⁺ (instead of its complex forms), through a two-pronged approach: on the one hand, achieving fast cathode redox kinetics by utilizing a heterogeneous enolization redox chemistry that avoids bond cleavage/re-formation; and on the other hand, improving bulk ion mobility and Mg²⁺ desolvation at the electrode surface with an electrolyte composed of a weakly coordinating anion in an ethereal solvent blend. We implemented both concepts by coupling an organic cathode material, pyrene-4,5,9,10-tetraone (PTO), with a modified MMC electrolyte solution with high solubility in a unique ethereal mixture, both of which exhibit outstanding properties: a specific capacity of 315 mAhg⁻¹ is recorded for PTO at a voltage of 2.1 V

¹Department of Electrical and Computer Engineering, University of Houston, Houston, TX, USA. ²Texas Center for Superconductivity at the University of Houston (TcSUH), Houston, TX, USA. ³Materials Research Department, Toyota Research Institute of North America, Ann Arbor, MI, USA. ⁴Advanced Light Source, Lawrence Berkeley National Laboratory, Berkeley, CA, USA. ⁵Department of Physics, Applied Physics and Astronomy, Binghamton University, Binghamton, NY, USA. ⁶These authors contributed equally: Hui Dong, Oscar Tutusaus. ✉e-mail: rana.mohtadi@toyota.com; yyao4@uh.edu

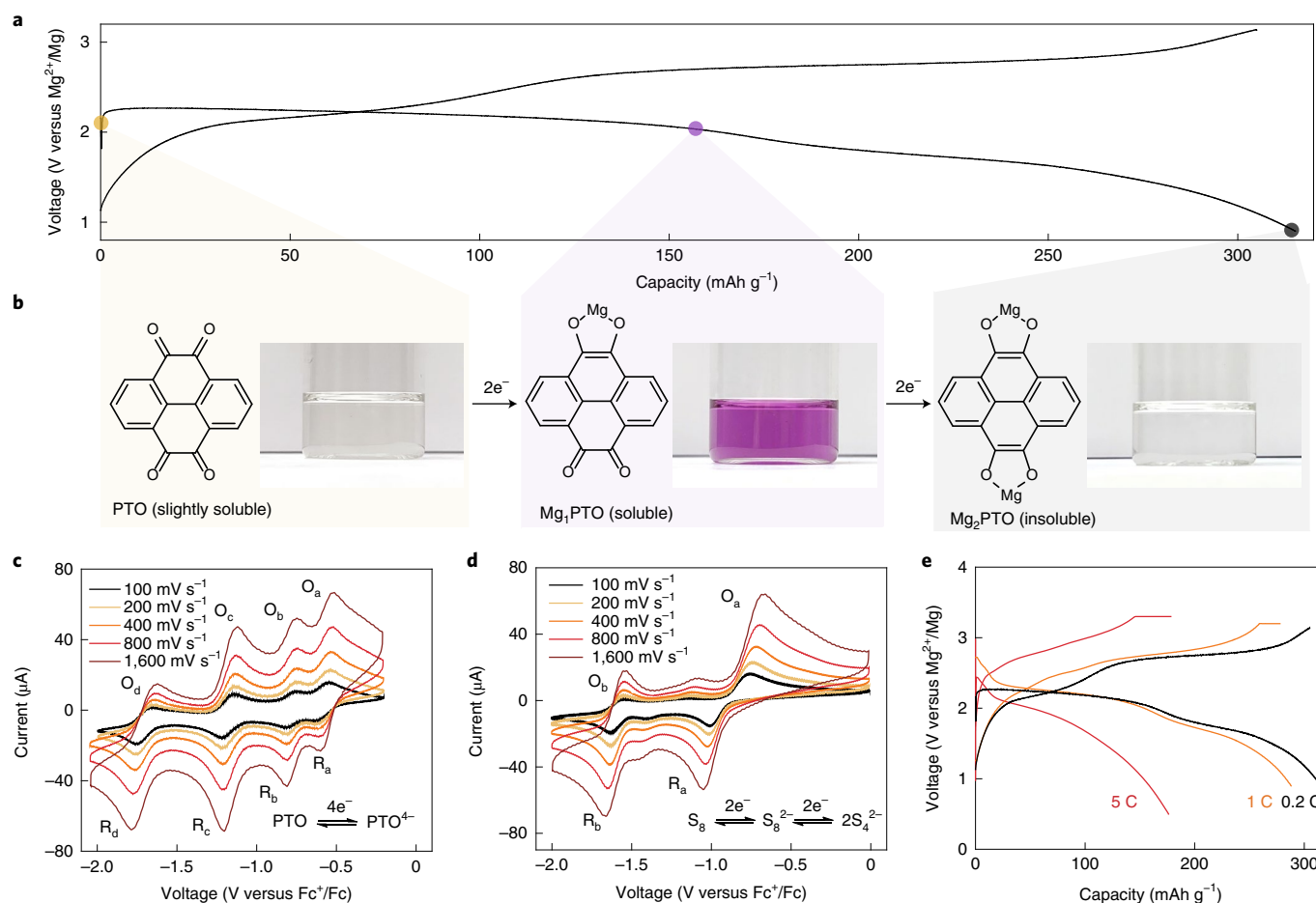


Fig. 1 | Proposed cathode heterogeneous enolization redox chemistry. **a**, Galvanostatic voltage profile of a Mg-PTO cell with MMC/G4 at 0.2 C ($1\text{C} = 408\text{ mA g}^{-1}$). **b**, Reductive enolization of PTO to Mg_1PTO and Mg_2PTO . The accompanying photographs of DME solutions of the electrodes at the corresponding states indicate the solubilities and colours of the intermediates. **c,d**, Cyclic voltammograms of 0.5 mM PTO (**c**) and S_8 (**d**) in a three-electrode setup using 0.1 M tetra-*n*-butylammonium perchlorate in acetonitrile. O, oxidation peak; R, reduction peak. **e**, Rate performance of Mg-PTO cells with MMC/G4 at 0.2, 1 and 5 C. Cells were tested under constant current-constant voltage (CC-CV) charging and constant current (CC) discharging modes; CV terminates when the current decays to 0.2 C. Broader voltage windows were applied for cells tested at higher C rates to compensate for the increasing overpotentials.

versus Mg^{2+}/Mg , and high current (20 mA cm^{-2}) dendrite-free Mg plating at an areal capacity of 3 mAh cm^{-2} is achieved with the modified MMC electrolyte. Our strategy culminates in a high-power Mg battery prototype that can be charged-discharged at up to 20 A g^{-1} and delivers a specific power of 30.4 kW kg^{-1} , which is close to two orders of magnitude higher than the current state-of-the-art Mg battery (0.45 kW kg^{-1}) (Supplementary Table 1).

Heterogeneous enolization redox chemistry

PTO was selected as a model cathode material to illustrate the heterogeneous enolization redox chemistry owing to its high theoretical specific capacity and solvent-free Mg^{2+} storage characteristics in chloride-free electrolytes (Supplementary Fig. 1). The electrochemical behaviour of PTO in MMC/G4 electrolyte was evaluated in a two-electrode Mg-PTO Swagelok cell. The voltage profile (Fig. 1a) consists of two discharge plateaus corresponding to two two-electron reductions, in agreement with the four carbonyl groups in a PTO molecule ($\text{C}=\text{O} \leftrightarrow \text{C}-\text{O}^-$). The observed specific capacity and average discharge voltage are 315 mAh g^{-1} and 2.03 V, respectively. Synchrotron-based soft X-ray absorption spectroscopy (sXAS) confirmed that the enolization redox reaction is indeed reversible (Supplementary Fig. 2a). X-ray photoelectron spectroscopy

(XPS) and inductively coupled plasma-optical emission spectroscopy (ICP-OES) measurements of discharged PTO electrodes revealed low atomic ratios of B:Mg of 2.12 and 2.54, respectively (Supplementary Fig. 2b). The results indicate that the stored species is Mg^{2+} rather than the anion-bound $\text{Mg}(\text{CB}_{11}\text{H}_{12})^+$, which has a ratio of 11:1. This finding prompted us to further study this cathode-electrolyte combination.

The cathode reaction mechanism of PTO was probed by optical characterizations. PTO electrodes at different states of discharge were extracted from the Swagelok cells and submerged in 1,2-dimethoxyethane (DME) solvent for three minutes. A half-discharged (2.0 V) electrode yields a purple solution (Fig. 1b), indicating that the reaction intermediate Mg_1PTO is soluble. A fully discharged (0.9 V) electrode gives a colourless solution, suggesting that the final discharge product, Mg_2PTO , is insoluble. The reduction of PTO can therefore be described as a heterogeneous liquid-solid reaction: the PTO is reduced to a soluble Mg_1PTO intermediate, then to the insoluble Mg_2PTO as the final product. Optical absorption measurements suggest ion-pair formation between Mg^{2+} and PTO^{2-} in the solution (Supplementary Fig. 3). The precipitation of Mg_2PTO indicates a spontaneous chemical process that overcomes the otherwise cumbersome solvent stripping from Mg^{2+} .

To fully understand the energy perspective of the solvation/desolvation process, molecular dynamics and thermodynamics calculations of the reaction products are required, which we will pursue and report separately in the future.

While the reaction of PTO resembles that of sulfur, a key difference manifests in the absence of covalent bond cleavage/re-formation in the enolization redox mechanism ($C=O \leftrightarrow C-O^-$) of PTO. This has important consequences for improving the redox kinetics and reversibility compared to conversion-type cathode materials such as sulfur, which suffer from irreversible and kinetically slow covalent bond cleavage and re-formation^{20–22}. To compare the intrinsic kinetic difference at the molecular level, we probed the electrochemical properties of dissolved PTO molecules in a 0.1 M tetra-*n*-butylammonium perchlorate solution (TBAClO₄) in acetonitrile due to its solubility, low viscosity and high conductivity, and compared it with that of sulfur (S₈) molecules. In cyclic voltammetry (CV), the peak potential separation (ΔE) between a pair of reduction and oxidation peaks is informative of the electrochemical reversibility and reaction kinetics²³. When a PTO molecule was reduced in the presence of non-interacting cations (TBA⁺), four reversible reduction waves were observed, indicating that four reduced species (presumably PTO⁻, PTO²⁻, PTO³⁻ and PTO⁴⁻) formed (Fig. 1c). The ΔE of these peaks (at 100 mV s⁻¹) ranges from around 65 to 92 mV, confirming high reversibility and intrinsically fast kinetics^{24,25}. The four waves show slightly different peak areas, which has been widely observed for quinones, and is attributed to the interplay between the rate constant difference of each step, parallel fast comproportionation reactions and surface adsorption^{26–28}. The PTO electrode tested in the Mg electrolyte (Fig. 1a) only displays two plateaus, with the four one-electron processes merging into two two-electron processes. The change may be explained by the strong interaction between Mg²⁺ and PTO^{-/2-} or Mg²⁺ and PTO^{3-/4-}, leading to the formation of ion pairs or even new phases. Okazaki and co-authors²⁹ and Abruña and co-authors³⁰ reported similar peak merging phenomena in the presence of Mg²⁺.

In contrast, two two-electron redox peaks are exhibited in S₈, in accordance with previous studies^{31,32}, and two redox peaks have been assigned to S₈ ↔ S₈²⁻ and S₈²⁻ → 2S₄²⁻ (Fig. 1d); ΔE values for the first and second reduction peaks are around 259 and 83 mV (at 100 mV s⁻¹), respectively, reflecting the much slower kinetics of S₈ than that of PTO. The diffusion coefficient (D) and rate constant (k) of PTO are higher than those of S₈ (Supplementary Table 2), also indicating the much faster kinetics of PTO. Furthermore, the maximum reduction of S₈ during solution CV measurements is 4 e⁻/S₈ (ref. ³²), which is dramatically lower than the 12–16 e⁻/S₈ observed from a long-term galvanostatic discharge of a solid electrode, while PTO shows 4 e⁻/PTO in both solution and solid cases. Notably, the kinetic advantage of PTO is also observed at the electrode level (Fig. 1e), where the specific capacities of a PTO electrode in a cell at 0.2, 1 and 5 C are 315, 288 and 176 mAh g⁻¹, respectively. This translates to a power density of 3,363 W kg⁻¹ at 5 C, surpassing the state-of-the-art power performance of Mg–S (445 W kg⁻¹) and Mg–Mo₆S₈ (270 W kg⁻¹ at 50 °C).

Practicality of heterogeneous enolization redox chemistry

Like other liquid–solid reaction-based batteries, a soluble reaction intermediate brings two concerns: cathode material loss caused by continuous dissolution upon cycling and passivation of the metal anode by the dissolved cathode species. Both of these issues were controlled effectively in our system. Although the PTO electrode does decay fast if the dissolution of PTO is left unattended (Supplementary Fig. 4), the decay has been efficiently mitigated by insertion of a thin (~2 μm) and lightweight (0.48 mg cm⁻²) graphene oxide (GO) membrane (Supplementary Fig. 5a,b) between the cathode and the separator to trap the intermediate (Fig. 2a), an approach that proved effective for Li–S batteries³³. The carboxyl groups on

GO act as ion-hopping sites of positively charged species (Li⁺; Mg²⁺) and reject the transport of negatively charged species (polysulfides; PTO²⁻) due to electrostatic interactions³³. Furthermore, GO flakes with two-dimensional structure also serve as physical barriers³³. After including a GO membrane, the reversible capacity reaches around 315 mAh g⁻¹ following an initial activation step, as a result of slow electrolyte penetration into the electrode due to the high viscosity of G4 (ref. ³⁴), and is stable for another 500 cycles with a capacity retention of around 84% (Fig. 2b and Supplementary Fig. 6). Note that the GO membrane (and the conductive carbon in the PTO electrode) has a negligible contribution to the cathode capacity (Supplementary Fig. 7) and that the average coulombic efficiency slightly above 100% could be ascribed to the shuttle effect caused by the dissolution of Mg₁PTO and imperfect confinement of the soluble PTO intermediate by the GO membrane.

On the other hand, the passivation of the Mg anode does not seem to apply to Mg–PTO batteries, despite being a known issue for Mg–S batteries caused by the trace amounts of dissolved polysulfides in the electrolyte solution³⁵. We have investigated Mg-plating behaviour in MMC/G4 electrolyte solutions with and without dissolved Mg₁PTO intermediate and found no notable variation in the overpotentials for deposition/stripping (Fig. 2c and Supplementary Fig. 8a). XPS characterization of the anode surface (Supplementary Fig. 8b) shows a signature for the Mg₂PTO product, but its presence did not negatively affect the Mg deposition/stripping process (Supplementary Fig. 8d). This behaviour contrasts with the plating/stripping process in MMC/G4 solutions containing soluble MgS₈ intermediate, where the overpotential almost doubled (Fig. 2d and Supplementary Fig. 8c), in agreement with previous reports³⁵.

Electrolytes with lower viscosity and weaker coordination

While the fast kinetics of the PTO cathode are demonstrated in our Mg–PTO cell, the cell power is still limited by the slow mass transport in the MMC/G4 electrolyte solution. We sought to exploit the full power capabilities of the PTO cathode by employing solvents that are less viscous and less coordinating than G4. Although many short-chain ethers meet these requirements, MMC has been found to display poor solubility in these solvents¹⁶. We have therefore explored solvent blends, a common practice in Li-ion battery electrolyte development, but still scarce within Mg battery research. Screening of ethereal solvent combinations revealed a cooperative effect between a narrow group of candidates that enable solubilization of MMC.

As shown in Fig. 3a, solubility of MMC was probed in 1:1 (v/v) blends of selected ether solvents using the available MMC solvates (see Methods sections ‘Preparation of Mg(CB₁₁H₁₂)₂ solvates’ and ‘Preparation of MMC electrolyte solutions’). Gratifyingly, a solubility enhancement was found in THF/DME, 1,3-dioxolane (DOL)/DME, DOL/diglyme (G2), THF/G2 and DME/G2 mixtures. These findings provide the key for overcoming the solubility limitations of MMC in less coordinating ethers^{18,19}. A thorough investigation of the solubility behaviour of MMC in THF, DME and G2 binary mixtures was undertaken at room temperature, where Fig. 3b and Supplementary Fig. 9a,b show the solubility diagrams of MMC in DME/G2, THF/DME and THF/G2 solvent blends. The most striking feature of these diagrams is that maximum solubility was reached at approximately 1:1 (w/w) solvent ratio regardless of solvent combination, with a maximum attainable MMC solubility of 0.55 mol kg⁻¹ for DME/G2, 0.37 mol kg⁻¹ for THF/DME and 0.82 mol kg⁻¹ for THF/G2 solvent blends, respectively.

Ionic conductivity dependence on MMC concentration in selected solvent mixtures was determined at 25 °C and is presented in Fig. 3c and Supplementary Fig. 9c. Satisfyingly, all these solvent mixtures improved over the previous values reported for G3 and G4 solutions¹⁶. Optimization of ionic conductivity within the available solubility space yielded 0.5 mol kg⁻¹ MMC/(DME–G2) (1:1, w/w)

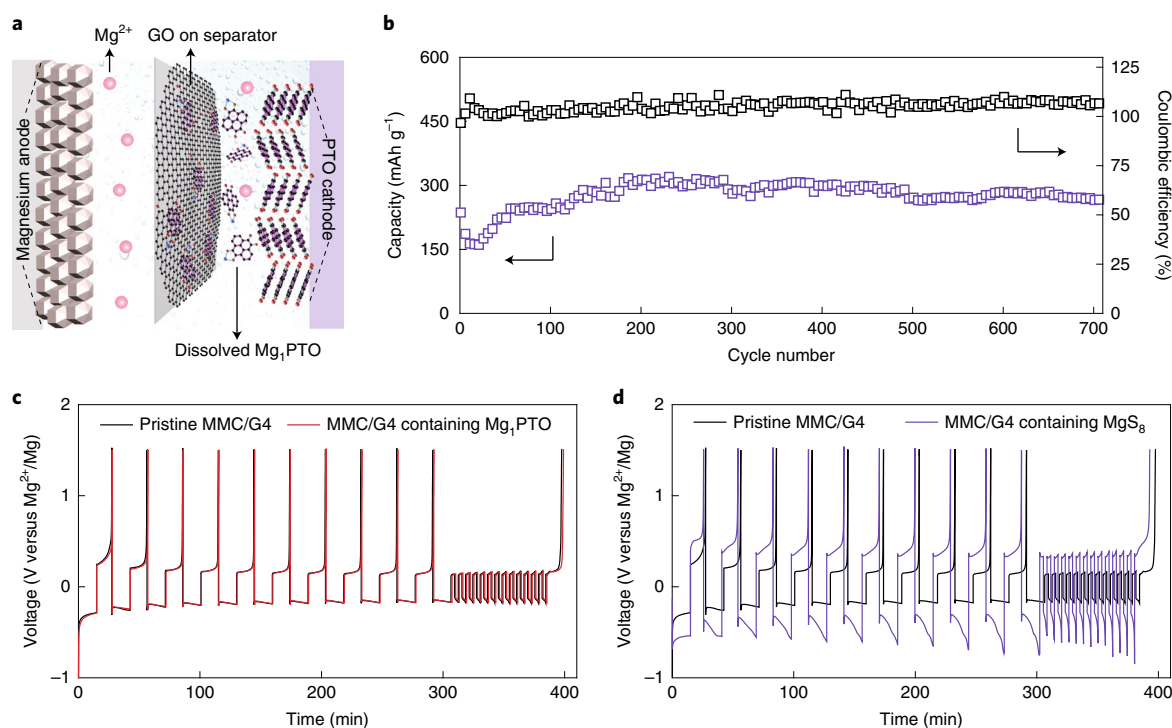


Fig. 2 | Practicality of heterogeneous enolization redox chemistry on cycling stability and anode reversibility. **a**, Schematic of a Mg-PTO cell with a thin ($\sim 2 \mu\text{m}$) and lightweight (0.48 mg cm^{-2}) GO membrane to mitigate the dissolution of Mg_1PTO intermediate in electrolyte. **b**, Cycling stability and coulombic efficiency of a GO-incorporated Mg-PTO cell cycled at the current density of 0.2 C ($1 \text{ C} = 408 \text{ mA g}^{-1}$). **c, d**, Voltage profiles of Mg|Cu asymmetric cells in pristine MMC/G4 electrolyte and that containing Mg_1PTO (**c**) or Mg_8S_3 (**d**).

as a superior candidate to MMC/G4, with an improved ionic conductivity of 6.1 mS cm^{-1} at 25°C . On the basis of these results, we selected 0.5 mol kg^{-1} MMC/(DME-G2) for further examination of the electrochemical properties. It is worth noting that use of solvent blends leads to a mixed-solvent shell of Mg^{2+} ions with a singular molecular structure not previously reported in any Mg electrolyte (Supplementary Fig. 10).

The modified electrolyte solution MMC/(DME-G2) substantially improves the kinetics of the Mg anode without compromising its coulombic efficiency (CE). Indeed, we confirmed an exceptional CE of 99.9% for MMC/(DME-G2) applying a method developed for Li metal³⁶ to accurately determine CE to a Mg|Cu asymmetric cell (see Methods and Supplementary Fig. 9d). Cyclic voltammetry of MMC/(DME-G2) in a three-electrode setup using a Pt disk as the working electrode (Fig. 3d) reveals a low overpotential ($<250 \text{ mV}$) for Mg plating, similar to that of MMC/G4. Of particular interest is that very high current densities are observed for Mg stripping, approaching 100 mA cm^{-2} , which is an order of magnitude higher than that for MMC/G4 and also higher than those for any reported Mg electrolytes^{17,37}. The observed fast electrode kinetics are consistent with the improved overall bulk transport properties of the electrolyte solution.

Dendrite-free Mg plating/stripping at high current densities

Galvanostatic cycling was conducted in Mg|Mg symmetric cells at four different current density values ($1, 5, 10$ and 50 mA cm^{-2}) (Supplementary Fig. 11). While both electrolytes are capable of cycling at an intermediate current density of 1 mA cm^{-2} , the overpotential for MMC/(DME-G2) ($\pm 39 \text{ mV}$) is dramatically lower than that of MMC/G4 ($\pm 97 \text{ mV}$). At high (10 mA cm^{-2}) and ultrahigh (50 mA cm^{-2}) current densities, the cell with MMC/(DME-G2) (Supplementary Fig. 11c) continues to cycle stably, while that with MMC/G4 is incapable of cycling even at

10 mA cm^{-2} (Supplementary Fig. 11b). The excellent rate performance is confirmed in Mg|Cu asymmetric cells in Fig. 3e. Remarkably, even at 50 mA cm^{-2} , MMC/(DME-G2) enables Mg deposition/stripping with a CE of 99.7%. The morphology of Mg deposited on Cu substrate at 20 mA cm^{-2} with areal capacity of 3 mAh cm^{-2} appears dense, smooth and dendrite-free (Fig. 3f). A symmetric Mg|Mg cell cycling under the same conditions remains stable after a cumulative capacity of 833 mAh cm^{-2} (Fig. 3g), which is far greater than that used in previously reported Mg|Mg symmetric cells (Supplementary Table 3). The smooth voltage profile indicates effective mass transport in the electrolyte solution so that the Sand's time is not exceeded. Our results consolidate Mg metal as a safe anode for advanced batteries even under demanding conditions.

Performance of high-power Mg batteries

Coupling the PTO cathode with MMC/(DME-G2) electrolyte yields a high-power Mg battery prototype. At a current density of 408 mA g^{-1} (1 C), two discharge plateaus become more obvious compared to cells with MMC/G4, and the average discharge voltage increases slightly to 2.1 V (Fig. 4a). Furthermore, the rate capability is improved substantially even at high C rates of 20 and 50 C, where specific capacities of 278 and 210 mAh g^{-1} can be retained, respectively. Stable cycling at 5 C for over 200 cycles with around 82% capacity retention (Fig. 4b and Supplementary Fig. 12) is achieved. This stability is enabled by a GO/graphene nanoparticle (GN) membrane (Supplementary Fig. 5c,d) with the necessary modification to simultaneously allow faster Mg^{2+} diffusion and confinement of soluble PTO intermediate³⁸. The CE is slightly above 100%, which we ascribe to the shuttle effect due to the dissolution of Mg_1PTO . The CE increased slightly with cycling because the soluble PTO intermediate dissolved gradually into the electrolyte and migrated to the anode side, due to the imperfect confinement of the GO/GN membrane.

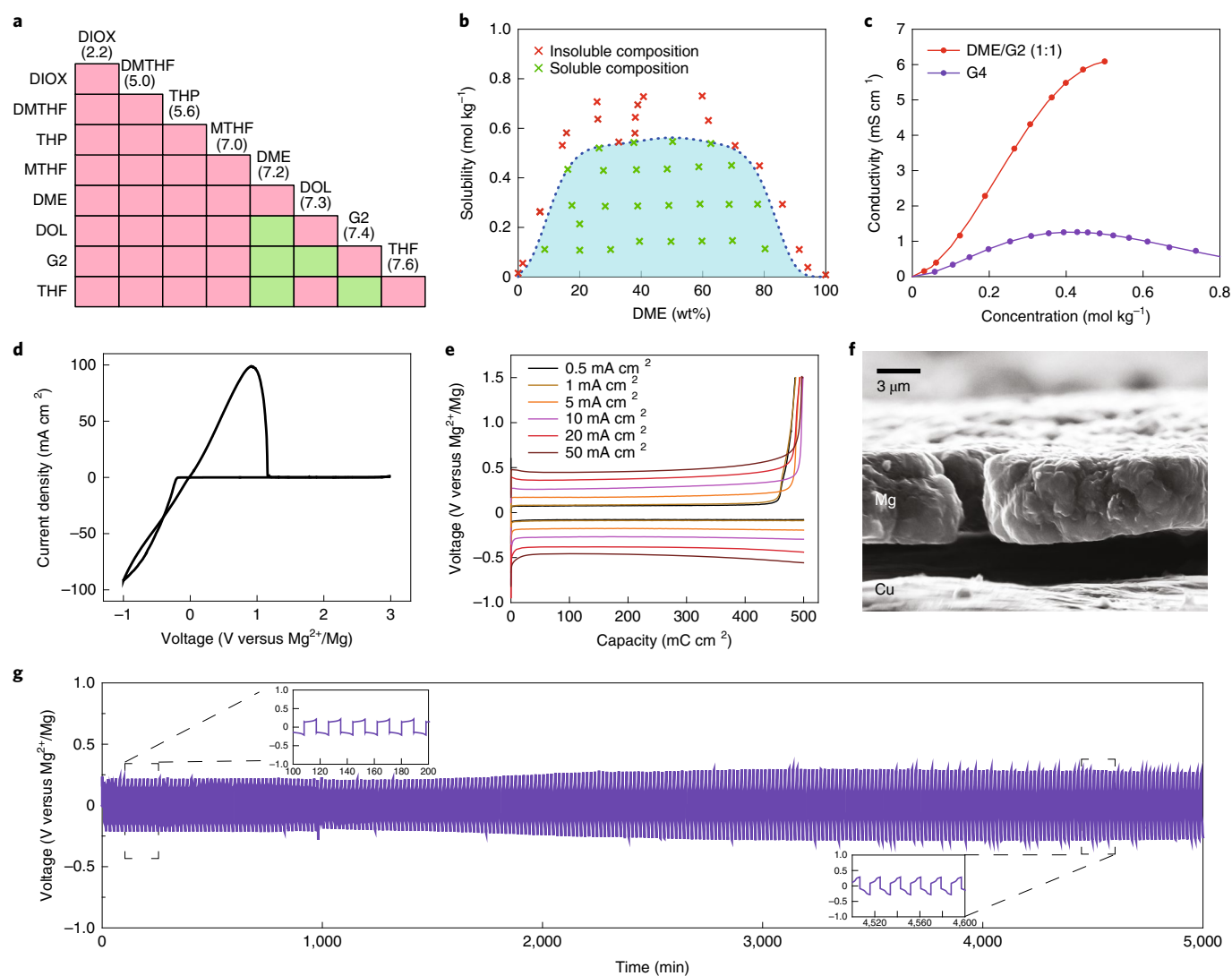


Fig. 3 | Design process and electrochemical performance of MMC/(DME-G2) electrolyte. a, Solubility chart of MMC at 0.3 mol kg⁻¹ level in 1:1 (v/v) etheral solvent blends (dielectric constants in parentheses). Colour code stands for solubility of MMC: pink (insoluble) and green (soluble). DIOX, 1,4-dioxane; DMTHF, 2,5-dimethyltetrahydrofuran; THP, tetrahydropyran; MTHF, 2-methyltetrahydrofuran; DME, 1,2-dimethoxyethane; DOL, 1,3-dioxolane; G2, diglyme; THF, tetrahydrofuran. **b**, Solubility diagram of MMC in the mixture of DME/G2. **c**, Ionic conductivity dependence on concentration of MMC solutions in G4 and DME/G2 mixture at 25 °C. **d**, Selected cyclic voltammogram for MMC/(DME-G2) on a Pt electrode at a scan rate of 35 mV s⁻¹. **e**, Polarizations of a Mg|Cu asymmetric cell at current densities from 0.5 to 50 mA cm⁻². **f**, Cross-sectional scanning electron microscopy image of Mg plated on a Cu substrate at 20 mA cm⁻² with areal capacity of 3 mAh cm⁻². **g**, Galvanostatic voltage profiles of a Mg|Mg symmetric cell cycled for plating/stripping 3 mAh cm⁻² per cycle at a current density of 20 mA cm⁻².

Finally, Fig. 4c compares the Ragone plot of state-of-the-art Mg metal batteries storing Mg²⁺ cations, and therefore excluding batteries storing complex ions, such as previously reported organic compounds, which have been shown to store either MgCl⁺ (in MgCl-based electrolytes) or solvated Mg²⁺ ions^{10,13,39}. Both intercalation-type cathodes (Mo₆S₈, Ti₃S₄) and conversion-type cathodes (S and I₂) display slow kinetics (up to 2C). In contrast, our cathode material relying on an enolization redox mechanism demonstrates a specific power of 30.4 kW kg⁻¹, a big increase from 0.45 kW kg⁻¹, which is the current highest power Mg battery²², while still providing a high material-level specific energy of 313 Wh kg⁻¹.

We note that since the aim of this work is to demonstrate heterogeneous enolization redox chemistry for Mg batteries, we have used a simple mixture of PTO and carbon for electrode fabrication. A high carbon content (50 wt%) was used to compensate for the low electronic conductivity (1.47 × 10⁻¹³ S cm⁻¹) of PTO

(Supplementary Fig. 13). Electrodes containing 50 wt% PTO, while still delivering an impressive specific energy of up to 446 Wh kg⁻¹ and a specific power of up to 29.2 kW kg⁻¹ (Supplementary Fig. 14), do not scale as well with increasing current density. Lean-electrolyte cell designs are also not practical for these highly porous electrodes, even though they are desirable for high cell-level-specific energy. We expect high PTO-content cathodes, and thus high cell-level-specific energy, when dedicated efforts are made to optimize these electrodes. All effective methods used in sulfur electrodes can be applied to PTO electrodes, such as complete encapsulation of active material in porous carbon host⁴⁰ and design of various carbon hosts with tailored nanostructures to increase electrical conductivity, with additional electron pathways and interconnected ion diffusion channels^{41,42}. Moreover, an electrode with low porosity by calendaring is also an essential condition to minimize electrolyte intake⁴³.

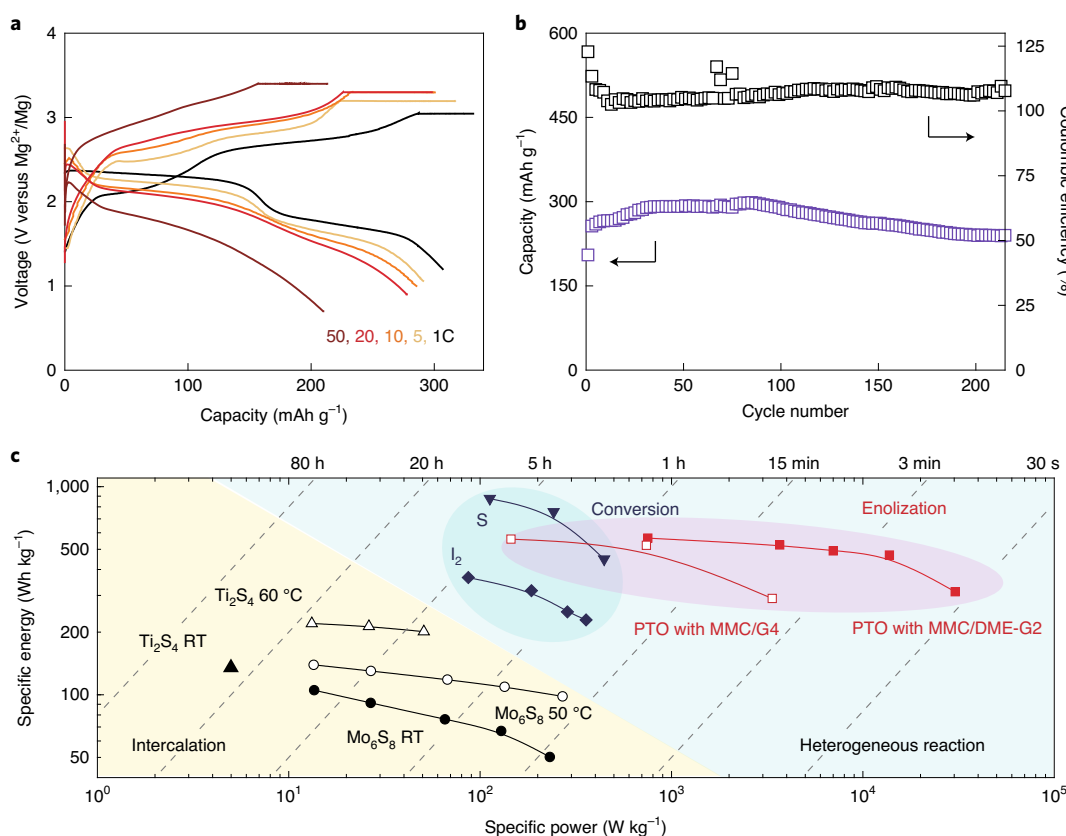


Fig. 4 | Electrochemical behaviour of Mg-PTO full cells in 0.5 mol kg⁻¹ MMC/(DME-G2) electrolyte. a, Voltage profiles of Mg-PTO cells at 1 to 50 C (1C = 408 mA g⁻¹) using CC-CV charging and CC discharging modes. CC-CV terminated when current density decayed to 0.5 C. Broader voltage windows were applied for cells tested at higher C rates to compensate for the increasing overpotentials. **b**, Cycling stability and coulombic efficiency of a GO/GN-incorporated Mg-PTO cell cycled at 5 C. **c**, Ragone plot of state-of-the-art Mg metal batteries that store Mg²⁺ ions. Calculation is based on the mass of cathode and anode active materials. RT, room temperature. The detailed parameters are summarized in Supplementary Table 1.

Conclusions

In this work, we have developed a high-power Mg battery featuring an organic quinone cathode with a tailored boron cluster-based electrolyte solution. The heterogeneous enolization redox chemistry holds the key to fast Mg²⁺ storage, and an electrolyte based on a weakly coordinating anion in an ethereal solvent mixture unlocks the potential of high-rate and dendrite-free Mg plating. Future work on tailoring the physical/chemical properties of the membrane could result in enhanced intermediate trapping and better cycling stability. Our results set directions for developing high-performance cathode materials and electrolyte solutions for Mg batteries, and unearth possibilities of using energy-dense metals for fast energy storage.

Methods

General. All experiments were conducted in an argon-filled glovebox, unless otherwise indicated. *n*-Butyl-*sec*-butylmagnesium in hexane was purchased from Acros Organics and used as received (note that di-*n*-butylmagnesium in heptane is also commercially available, but we avoided using the latter because it contains between 1% and 5% of triethylaluminium). Magnesium bis(hexamethyldisilazide) (MgHMDS, 97%) was purchased from Sigma-Aldrich and used as received. [HNEt₃][CB₁₁H₁₂] was purchased from Katchem and used as received. 2,5-Dimethyltetrahydrofuran (DMTHF, 1:1 mixture of *cis* and *trans*) was purchased from TCI and dried over activated 3-Å molecular sieves before use. Hexane, 2-methyltetrahydrofuran (MTHF), 1,3-dioxolane (DOL), tetrahydropyran (THP) and 1,4-dioxane (DIOX) were purchased in anhydrous form from Sigma-Aldrich and stored over activated 3-Å molecular sieves before use. Tetrahydrofuran (THF), 1,2-dimethoxyethane (DME) and diglyme (G2) were purchased in anhydrous form from Sigma-Aldrich, distilled from Na metal and stored over activated 3-Å molecular sieves. Triglyme (G3) and tetraglyme (G4)

were purchased from Sigma-Aldrich, distilled from Na metal and stirred in the presence of freshly prepared Mg shavings at 100 °C for 15 h, whereupon they were stored until used.

Preparation of Mg(CB₁₁H₁₂)₂ solvates. Preparation of [Mg(DME)₃](CB₁₁H₁₂)₂: this solvate was prepared according to the literature⁴⁴.

Preparation of [Mg(G2)₂](CB₁₁H₁₂)₂:G2: this solvate was prepared according to the literature¹⁶.

Preparation of [Mg(THF)₆](CB₁₁H₁₂)₂: (HNEt₃)CB₁₁H₁₂ (250.8 mg, 1.02 mmol) was dissolved in anhydrous THF (3 ml) and filtered. The clear filtrate was placed in a scintillation vial and 0.7 ml (0.55 mmol) of MgBu₂ (0.78 M solution in hexanes) was added dropwise with efficient stirring. A white solid precipitated and the mixture warmed up due to exothermic reaction. The suspension was stirred for 45 min and filtered. The white solid was washed with THF (3 × 2 ml) and dried under vacuum until constant weight. Yield: 363.6 mg (96%). NMR characterization matched that reported previously¹⁶.

Preparation of other Mg(CB₁₁H₁₂)₂ solvates ([Mg(Me-THF)₄](CB₁₁H₁₂)₂, [Mg(Me₂-THF)₄](CB₁₁H₁₂)₂, [Mg(DOL)₂](CB₁₁H₁₂)₂, [Mg(THP)₃](CB₁₁H₁₂)₂ and [Mg(DIOX)₃](CB₁₁H₁₂)₂) are included in the Supplementary information.

Preparation of MMC electrolyte solutions. Preparation of 0.5 mol kg⁻¹ Mg(CB₁₁H₁₂)₂ in G4 (MMC/G4) electrolyte: [Mg(DME)₃](CB₁₁H₁₂)₂ (1.000 g) was dissolved in anhydrous G4 (3.447 ml) with stirring and the resulting clear solution was vigorously stirred under vacuum to remove DME solvent.

Preparation of 0.5 mol kg⁻¹ Mg(CB₁₁H₁₂)₂ in DME-G2 (1:1, w/w) electrolyte: [Mg(DME)₃](CB₁₁H₁₂)₂ (1.000 g) was added to anhydrous DME (1.256 g) and anhydrous G2 (1.722 g) and the mixture stirred at room temperature until a clear solution was obtained.

Other MMC electrolyte solutions: [Mg(THF)₆](CB₁₁H₁₂)₂ solvate was used to prepare MMC/(THF-G2) electrolyte. [Mg(DME)₃](CB₁₁H₁₂)₂ solvate was used to prepare MMC/(THF-DME), MMC/(DME-G2), MMC/(DOL-DME) and MMC/G4 electrolyte. [Mg(G2)₂](CB₁₁H₁₂)₂:G2 solvate was used to prepare MMC/(DOL-G2) electrolyte.

Solubility test and electrolyte conductivity measurements. A weighed amount of $\text{Mg}(\text{CB}_{11}\text{H}_{12})_2$ solvate was added to a tared 2-ml vial containing a stir bar and the vial was capped with a septum-lined cap. A weighed amount of a selected first solvent (typically the same solvent as that in the solvate salt) was added with a syringe and the mixture stirred for about 10 s. A selected second solvent was added dropwise with a syringe while stirring until dissolution. When most of the solid had dissolved, the mixture was stirred for a minimum of 1 min following each addition to ensure equilibrium was reached.

Liquid electrolyte conductivity was measured at $25 \pm 0.5^\circ\text{C}$ (controlled by an IKA heating plate) using the a.c. impedance technique with a Bio-Logic VMP3 multichannel potentiostat that included frequency response analyser modules. A custom-made electrochemical cell was utilized consisting of two polished Pt disk electrodes (1.6 mm in diameter) embedded at the bottom of a polytetrafluoroethylene (PTFE) plastic body rod (7.5 cm length \times 6 mm outer diameter), and with both rods positioned parallel such that the Pt discs were at the same level. The cell constant was determined by measuring a standard KCl solution beforehand to test solutions.

Preparation of electrodes. PTO was synthesized following a previous report⁴⁵. For all experiments in this work unless otherwise indicated, PTO, Ketjenblack carbon (KB) and PTFE binder were mixed in a 3:5:2 mass ratio with the aid of ethanol and pressed to form freestanding electrodes with an areal mass loading of PTO as $\sim 2.5 \text{ mg cm}^{-2}$. For the experiments of Mg anode study, sXAS, XPS, ICP, UV–visible spectroscopy and Fourier transform infrared measurements, PTO, KB and PTFE binder were mixed in a 6:3:1 mass ratio and the areal mass loading of PTO was $\sim 5 \text{ mg cm}^{-2}$. The electrodes were dried at 85°C under vacuum for 24 h.

P14AQ was synthesized as reported⁴⁶. P14AQ, KB and PTFE binder were mixed in a 6:3:1 ratio and the areal mass loading of P14AQ in the electrode was $\sim 5 \text{ mg cm}^{-2}$. The electrodes were dried at 100°C under vacuum for 6 h. Sulfur was purchased from Sigma-Aldrich and used without further purification. KB and sulfur were hand mixed in a 6:3 mass ratio and heated at 155°C for 24 h to allow sulfur infiltration into KB. The S–KB composite was then mixed with PTFE at a mass ratio of 9:1 to form freestanding electrodes with the areal mass loading of sulfur being $\sim 5 \text{ mg cm}^{-2}$. The electrodes were dried at 50°C under vacuum for 6 h.

Electrochemical measurements. All experiments were conducted at room temperature, using a potentiostat (VMP3, Bio-Logic) or a battery tester (LAND CT-2001A). All cells were assembled and tested in an argon-filled glovebox (M-Braun, <0.5 ppm of water and oxygen). Mg foil (50 μm thick, 99.995%, GalliumSource) was polished before use and Cu foil was washed with acetone before use. Two-electrode Swagelok cells (molybdenum rods as the current collectors) and glass fibre separators were used for all electrochemical characterizations unless otherwise indicated. For a Mg|Mg symmetric cell, two Mg foils were used. For a Mg|Cu asymmetric cell, a Mg foil was used as a counter electrode and a Cu foil served as a substrate for Mg deposition. We followed the protocol of Method 3 reported by Zhang and co-authors for accurate determination of electrolyte CE³⁶. It is necessary to introduce a stabilization process before the measurement of Mg CE. Q_i is the initial amount of charge deposited on to the Cu substrate as a Mg reservoir, then a smaller portion of this charge (Q_c) is used to cycle Mg between working and counter electrodes for n cycles. After n cycles, a final exhaustive strip of the remaining Mg reservoir is performed to the cut-off voltage. The final stripping charge (Q_f) was measured. The average CE can be calculated as $(nQ_c + Q_i)/(nQ_c + Q_f)$. In all experiments, the Cu substrate was preconditioned with 10 cycles of Mg plating/stripping at a current density of 0.5 mA cm^{-2} for 15 min of plating and stripping until reaching the voltage cut-off of 1.5 V versus Mg/Mg^{2+} . Afterwards, Mg was deposited for another 15 min (Q_i), followed by 13 cycles of 3 min stripping and 3 min plating (Q_c) per cycle, before a final complete stripping (Q_f). For a Mg–PTO (or Mg–S or Mg–P14AQ) full-cell, a Mg foil was used as an anode and a PTO (or S or P14AQ) electrode was used as a cathode. The cells presented in this work used a flooded-electrolyte ($>100 \mu\text{l mg}^{-1}$ of PTO) design. For a GO (or GO/GN)-incorporated Mg–PTO full-cell, a freestanding GO (or GO/GN) membrane was sandwiched between the PTO cathode and the separator. The cyclic voltammetry experiment of the Mg electrolyte was conducted at a scan rate of 35 mV s^{-1} in a three-electrode cell using a Pt disk as the working electrode, and Mg ribbons were used as reference and counter electrodes. Cyclic voltammetry of 0.5 mM sulfur or PTO acetonitrile solution containing 0.1 M tetra- n -butylammonium perchlorate was conducted in a three-electrode cell using a glassy carbon working electrode, a Pt wire as a pseudo-reference electrode and a Pt disk as the counter electrode. iR compensation was applied for the CV curves. The ferrocene/ferrocenium couple (2 mM) was used as an internal reference.

Preparation of GO and GO/GN membranes. The GO film was prepared by dispersing 6 mg GO powder in 20 ml of ethanol by a sonifier (450 Digital Sonifier, Branson) for 30 min. The suspension was filtered through the Celgard separator to obtain a freestanding film and dried under vacuum at 80°C overnight. The GO/GN film was prepared by first dispersing 2 mg GN (XG Science) in 20 ml ethanol by a sonifier (450 Digital Sonifier, Branson) for 30 min. Then, 4 mg GO powder (ACS Material) was added into the suspension and ultrasonicated for another

30 min. The suspension was filtered through a Celgard separator to obtain a freestanding film and dried under vacuum at 80°C overnight. The areal loading for both films was 0.48 mg cm^{-2} .

Materials characterizations. The discharged and recharged PTO electrodes were characterized by XPS (Physical Electronics Model 5700), ICP–OES (Agilent Technologies, Model 725), sXAS and Fourier transform infrared spectroscopy. sXAS was performed in an iRIXS endstation at beamline 8.0.1 of the Advanced Light Source⁴⁷. The energy resolution was better than 0.2 eV without considering core hole lifetime broadening. Particularly for the experiments here, radiation damage was reduced by tuning three experimental parameters: a defocused large beam size of more than $500 \times 500 \mu\text{m}^2$, decreased X-ray flux of the incident beam through controlled slit sizes and cooling down the samples by liquid N_2 . All the samples were maintained under inert gas system throughout the sample transfer process to avoid air exposure. Incident beam flux was measured simultaneously at each sXAS data spot and was used for spectral normalization. The sXAS data shown were collected through the total fluorescence yield mode with a relatively deeper probe depth of about 100 nm for the O–K edge. Infrared spectra were performed as single-reflection attenuated total reflectance measurements with powder samples using a Thermo Scientific Nicolet iS 5 instrument. All electrodes were extracted from disassembled cells in an Ar-filled glovebox and washed by dipping in anhydrous DME (3 min and three times). The washed electrodes were vacuum-dried at room temperature for 30 min and ground in an agate mortar with a pestle to avoid measuring only the electrode surface. The UV–visible absorption spectra of the diluted DME solutions containing the electrolytes extracted from the tubular cell at different states of discharge were measured using a spectrophotometer (Cary 60, Agilent Technologies). Scanning electron microscopy was conducted using a Gemini LEO 1525 microscope. Before analysis, the Cu electrode was first rinsed with DME solvent three times to remove residual electrolytes and vacuum-dried at room temperature. The cross-section of Cu electrode with Mg deposition was prepared by cutting the electrode with a scissor, which led to a gap between deposited Mg and the Cu substrate as shown in Fig. 3f. NMR analyses were conducted on Varian MR 400 MHz, Varian VNMR5 500 MHz and Varian VNMR5 700 MHz spectrometers. ^1H and ^{13}C NMR spectra were referenced relative to the solvent peak, and ^{11}B spectra were referenced indirectly on the basis of the ^1H spectra⁴⁸.

Data availability

The authors declare that the data supporting the findings of this study are available within the article and its Supplementary Information files.

Received: 1 July 2020; Accepted: 3 November 2020;

Published online: 30 November 2020

References

- Liang, Y., Dong, H., Aurbach, D. & Yao, Y. Current status and future directions of multivalent metal-ion batteries. *Nat. Energy* **5**, 646–656 (2020).
- Yoo, H. D. et al. Mg rechargeable batteries: an on-going challenge. *Energy Environ. Sci.* **6**, 2265–2279 (2013).
- Choi, J. W. & Aurbach, D. Promise and reality of post-lithium-ion batteries with high energy densities. *Nat. Rev. Mater.* **1**, 16013 (2016).
- Suo, L. et al. ‘Water-in-salt’ electrolyte enables high-voltage aqueous lithium-ion chemistries. *Science* **350**, 938–943 (2015).
- Attias, R., Salama, M., Hirsch, B., Goffer, Y. & Aurbach, D. Anode-electrolyte interfaces in secondary magnesium batteries. *Joule* **3**, 27–52 (2019).
- Mohtadi, R. & Mizuno, F. Magnesium batteries: current state of the art, issues and future perspectives. *Beilstein J. Nanotechnol.* **5**, 1291–1311 (2014).
- Wan, L. F., Perdue, B. R., Appleby, C. A. & Prendergast, D. Mg desolvation and intercalation mechanism at the Mo_6S_8 chevrel phase surface. *Chem. Mater.* **27**, 5932–5940 (2015).
- Canepa, P. et al. Odyssey of multivalent cathode materials: open questions and future challenges. *Chem. Rev.* **117**, 4287–4341 (2017).
- Sun, X. et al. A high capacity thiospinel cathode for Mg batteries. *Energy Environ. Sci.* **9**, 2273–2277 (2016).
- Dong, H. et al. Directing Mg-storage chemistry in organic polymers toward high-energy Mg batteries. *Joule* **3**, 782–793 (2019).
- Li, Z. et al. Fast kinetics of multivalent intercalation chemistry enabled by solvated magnesium-ions into self-established metallic layered materials. *Nat. Commun.* **9**, 5115 (2018).
- Yoo, H. D. et al. Fast kinetics of magnesium monochloride cations in interlayer-expanded titanium disulfide for magnesium rechargeable batteries. *Nat. Commun.* **8**, 339 (2017).
- Fan, X. et al. A universal organic cathode for ultrafast lithium and multivalent metal batteries. *Angew. Chem. Int. Ed. Engl.* **57**, 7146–7150 (2018).
- Kim, H. et al. Sodium intercalation chemistry in graphite. *Energy Environ. Sci.* **8**, 2963–2969 (2015).
- Aurbach, D. et al. Prototype systems for rechargeable magnesium batteries. *Nature* **407**, 724–727 (2000).

16. Tutusaus, O. et al. An efficient halogen-free electrolyte for use in rechargeable magnesium batteries. *Angew. Chem. Int. Ed. Engl.* **54**, 7900–7904 (2015).
17. Zhao-Karger, Z., Gil Bardaji, M. E., Fuhr, O. & Fichtner, M. A new class of non-corrosive, highly efficient electrolytes for rechargeable magnesium batteries. *J. Mater. Chem. A* **5**, 10815–10820 (2017).
18. Shao, Y. et al. Nanocomposite polymer electrolyte for rechargeable magnesium batteries. *Nano Energy* **12**, 750–759 (2015).
19. Rajput, N. N., Seguin, T. J., Wood, B. M., Qu, X. & Persson, K. A. Elucidating solvation structures for rational design of multivalent electrolytes—a review. *Top. Curr. Chem.* **376**, 19 (2018).
20. Yamin, H. Lithium sulfur battery. *J. Electrochem. Soc.* **135**, 1045 (1988).
21. Merritt, M. V. & Sawyer, D. T. Electrochemical reduction of elemental sulfur in aprotic solvents. Formation of a stable S_8^- species. *Inorg. Chem.* **9**, 211–215 (1970).
22. Du, A. et al. An efficient organic magnesium borate-based electrolyte with non-nucleophilic characteristics for magnesium–sulfur battery. *Energy Environ. Sci.* **10**, 2616–2625 (2017).
23. Huang, X. et al. Cyclic voltammetry in lithium–sulfur batteries—challenges and opportunities. *Energy Technol.* **7**, 1801001 (2019).
24. Suga, T., Pu, Y.-J., Oyaizu, K. & Nishide, H. Electron-transfer kinetics of nitroxide radicals as an electrode-active material. *Bull. Chem. Soc. Jpn.* **77**, 2203–2204 (2004).
25. Martínez-Cifuentes, M., Salazar, R., Ramírez-Rodríguez, O., Weiss-López, B. & Araya-Maturana, R. Experimental and theoretical reduction potentials of some biologically active ortho-carbonyl para-quinones. *Molecules* **22**, 577 (2017).
26. Rüssel, C. & Janicke, W. Heterogeneous electron exchange of quinones in aprotic solvents: part III. The second reduction step of *p*-benzoquinone and its dependence on the supporting electrolyte. *J. Electroanal. Chem. Interf. Electrochem.* **199**, 139–151 (1986).
27. Lehmann, M. W. & Evans, D. H. Anomalous behavior in the two-step reduction of quinones in acetonitrile. *J. Electroanal. Chem.* **500**, 12–20 (2001).
28. Nikitina, V. A., Nazmutdinov, R. R. & Tsilina, G. A. Quinones electrochemistry in room-temperature ionic liquids. *J. Phys. Chem. B* **115**, 668–677 (2011).
29. Oyama, M., Hoshino, T. & Okazaki, S. Solvent effect on the ion pair formation between 2,3,5,6-tetrachloro-1,4-benzoquinone anion radical and Mg^{2+} measured using a pulse electrolysis stopped flow method. *J. Electroanal. Chem.* **401**, 243–246 (1996).
30. Hernández-Burgos, K., Rodríguez-Calero, G. G., Zhou, W., Burkhardt, S. E. & Abruña, H. D. Increasing the gravimetric energy density of organic based secondary battery cathodes using small radius cations (Li^+ and Mg^{2+}). *J. Am. Chem. Soc.* **135**, 14532–14535 (2013).
31. Martin, R. P., Doub, W. H., Roberts, J. L. & Sawyer, D. T. Electrochemical reduction of sulfur in aprotic solvents. *Inorg. Chem.* **12**, 1921–1925 (1973).
32. Lu, Y.-C., He, Q. & Gasteiger, H. A. Probing the lithium–sulfur redox reactions: a rotating-ring disk electrode study. *J. Phys. Chem. C* **118**, 5733–5741 (2014).
33. Huang, J.-Q. et al. Permsselective graphene oxide membrane for highly stable and anti-self-discharge lithium–sulfur batteries. *ACS Nano* **9**, 3002–3011 (2015).
34. Tian, J., Zhou, X., Wu, Q. & Li, C. Li-salt mediated Mg-rhodizonate batteries based on ultra-large cathode grains enabled by K-ion pillaring. *Energy Storage Mater.* **22**, 218–227 (2019).
35. Salama, M. et al. On the feasibility of practical Mg–S batteries: practical limitations associated with metallic magnesium anodes. *ACS Appl. Mater. Interfaces* **10**, 36910–36917 (2018).
36. Adams, B. D., Zheng, J., Ren, X., Xu, W. & Zhang, J.-G. Accurate determination of coulombic efficiency for lithium metal anodes and lithium metal batteries. *Adv. Energy Mater.* **8**, 1702097 (2018).
37. Luo, J., Bi, Y., Zhang, L., Zhang, X. & Liu, T. L. A stable, non-corrosive perfluorinated pinacolborate Mg electrolyte for rechargeable Mg batteries. *Angew. Chem. Int. Ed. Engl.* **58**, 6967–6971 (2019).
38. Wang, W. et al. Graphene oxide membranes with tunable permeability due to embedded carbon dots. *Chem. Commun.* **50**, 13089–13092 (2014).
39. Bitenc, J., Vizintin, A., Grdadolnik, J. & Dominko, R. Tracking electrochemical reactions inside organic electrodes by operando IR spectroscopy. *Energy Storage Mater.* **21**, 347–353 (2019).
40. Gueon, D., Ju, M.-Y. & Moon, J. H. Complete encapsulation of sulfur through interfacial energy control of sulfur solutions for high-performance Li–S batteries. *Proc. Natl Acad. Sci. USA* **117**, 12686–12692 (2020).
41. Li, Z., Zhang, J. T., Chen, Y. M., Li, J. & Lou, X. W. Pie-like electrode design for high-energy density lithium–sulfur batteries. *Nat. Commun.* **6**, 8850 (2015).
42. Pei, F. et al. Self-supporting sulfur cathodes enabled by two-dimensional carbon yolk-shell nanosheets for high-energy-density lithium-sulfur batteries. *Nat. Commun.* **8**, 482 (2017).
43. Kang, N. et al. Cathode porosity is a missing key parameter to optimize lithium-sulfur battery energy density. *Nat. Commun.* **10**, 4597 (2019).
44. Singh, N. et al. Achieving high cycling rates via in situ generation of active nanocomposite metal anodes. *ACS Appl. Energy Mater.* **1**, 4651–4661 (2018).
45. Liang, Y. et al. Universal quinone electrodes for long cycle life aqueous rechargeable batteries. *Nat. Mater.* **16**, 841–848 (2017).
46. Pan, B. et al. Polyanthraquinone-based organic cathode for high-performance rechargeable magnesium-ion batteries. *Adv. Energy Mater.* **6**, 1600140 (2016).
47. Qiao, R. et al. High-efficiency in situ resonant inelastic X-ray scattering (iRIXS) endstation at the Advanced Light Source. *Rev. Sci. Instrum.* **88**, 033106 (2017).
48. Harris, R. K., Becker, E. D., Cabral de Menezes, S. M., Goodfellow, R. & Granger, P. NMR nomenclature: nuclear spin properties and conventions for chemical shifts: IUPAC recommendations 2001. *Solid State Nucl. Magn. Reson.* **22**, 458–483 (2002).

Acknowledgements

Y.Y. acknowledges the support of University of Houston. R.M. and O.T. acknowledge the funding provided from Toyota Motor Corporation. This research used resources of the Advanced Light Source, which is a DOE Office of Science User Facility under contract no. DE-AC02-05CH11231. We acknowledge K. Suto, Y. Kotani, F. Mizuno, T. Matsunaga and H. Aso from Toyota Motor Corporation and K. Takechi from Toyota Central R&D, N. Singh, T. A. Arthur, R. Sugiura, P. Fanson and T. Inoue at Toyota Research Institute of North America for support and discussion.

Author contributions

H.D., O.T., Y.L., R.M. and Y.Y. conceived and designed the experiments. O.T. and R.M. synthesized the electrolytes. H.D. synthesized and fabricated organic electrodes. H.D., O.T. and Y.Z. performed electrochemical and materials characterizations. H.D. and Y.Z. prepared GO membranes. W.Y. and Z.L.-H. performed soft X-ray absorption spectroscopy measurements. H.D., O.T., Y.L., R.M. and Y.Y. wrote the manuscript. R.M. and Y.Y. supervised the project.

Competing interests

R.M. is inventor on US Patent 9240613 and O.T. and R.M. are inventors on US Patents 9252458 and 20180151917, which are assigned to Toyota Motor Engineering & Manufacturing North America, Inc. Y.Y., H.D. and Y.L. are inventors on US Patent 63043240. O.T. and R.M. are employees of Toyota Research Institute of North America, the research division at Toyota Motor Engineering & Manufacturing North America (TEMA), Inc.

Additional information

Supplementary information is available for this paper at <https://doi.org/10.1038/s41560-020-00734-0>.

Correspondence and requests for materials should be addressed to R.M. or Y.Y.

Peer review information *Nature Energy* thanks Vinayan Bhagavathi Parambath, Niya Sa and the other, anonymous, reviewer(s) for their contribution to the peer review of this work.

Reprints and permissions information is available at www.nature.com/reprints.

Publisher's note Springer Nature remains neutral with regard to jurisdictional claims in published maps and institutional affiliations.

© The Author(s), under exclusive licence to Springer Nature Limited 2020